

Non-Spin Torque Origin of Current-Induced Switching in an Antiferromagnet Insulator/Pt Bilayer Film

Pengxiang Zhang¹, Joseph Finley¹, Taqiyyah Safi¹, Jiahao Han¹ and Luqiao Liu^{1*}

¹Department of Electrical Engineering and Computer Science, Massachusetts Institute of Technology, Cambridge, MA 02139, USA

*email: luqiao@mit.edu

Electrical control and detection of magnetic ordering inside antiferromagnets has attracted considerable interests, for the potential advantages in operating speed and device densities. In contrast to ferromagnets, where the current induced torque on magnetic moments was first established and quantified via comparison with magnetic field's influence, the investigation on the spin torque mechanism in antiferromagnets represents a greater challenge, due to the lack of an independent method for controlling Néel vectors. Here by utilizing an antiferromagnetic insulator with Dzyaloshinskii-Moriya interaction, α -Fe₂O₃, we show that the Néel vector can be conveniently controlled with the application of a moderate external magnetic field, which is further used to examine the current-induced magnetic dynamics. We find that the switching criteria employed in many of the previous studies -- the sawtooth feature in resistance or Hall resistance change is not necessarily related to the reorientation of Néel order. By further comparing the current and field-induced Néel vector tilting and through a systematic scaling study, we reveal the important role of magnetoelastic effect in current induced switching of this antiferromagnet. The spin torque effect induced

switching, which is expected to be smaller and has the opposite sign as the magnetoelastic effect in our experiment, remains yet to be demonstrated.

Current induced magnetic switching has been recently reported in both metallic¹⁻⁷ and insulating⁸⁻¹¹ antiferromagnetic systems. So far, anisotropic magnetoresistance (AMR), spin Hall magnetoresistance (SMR) or related planar Hall resistance (PHR) has been generally employed to characterize the electrically induced 90° Néel vector switching. In these studies, the antiferromagnetic switching is usually demonstrated with a series of current pulses applied along orthogonal directions, which reversibly set and reset the Hall cross resistance at high and low values. Very often the relative change of resistance values in these switching experiments are gradually saturated after a long sequence of pulses. In the meantime, the switchings can be suppressed over repeated writing cycles. All of these features are in sharp contrast to the fast, single-pulse-induced, fully repeatable ferromagnetic switchings observed previously¹²⁻¹⁴. Moreover, unlike ferromagnetic system, where the current induced spin torque can be calibrated by using the external magnetic field as a standard, it is much less straightforward to build the correspondence between the magnetic ordering orientation and the resistance value change in experiments with antiferromagnet. Except in a few studies^{2,7,8,10}, where the current induced antiferromagnetic domain switching is observed through X-ray based imaging techniques, the correlation between the observed resistance change and the reorientation of magnetic ordering remains to be established. Therefore, there is an urgent need for developing an electrical measurement method that can provide non-spurious evidence on the existence of spin torque, as well as quantitatively determine its magnitude in antiferromagnets.

α -Fe₂O₃ is a well-studied antiferromagnetic insulator¹⁵⁻¹⁷, with high Néel temperature (955 K) and strong antiferromagnetic exchange interaction (effective exchange field ~ 900 T). As is shown in Fig. 1a, α -Fe₂O₃ has trigonal crystal structure, and the two spin sublattices are stacked alternatively along (0001) direction. It is well-known¹⁸ that at room temperature, α -Fe₂O₃ exhibits

an easy-plane anisotropy, which has a very weak ferromagnetism ($M_s \sim 2$ emu/cc) due to the Dzyaloshinskii-Moriya (DM) interaction that causes a $< 0.1^\circ$ in-plane canting angle between magnetic moments of the two sub-lattices. Thanks to the small net moment and the very weak magnetic anisotropy within the basal plane¹⁸, the spin-flop field for aligning the Néel vector perpendicular to the external field direction in α -Fe₂O₃ can be orders of magnitude smaller compared with regular antiferromagnets, providing a convenient way for controlling the magnetic ordering orientation. In the meantime, the small net moment (\mathbf{M}) is perpendicularly oriented with respect to the Néel vector (\mathbf{N}) direction, allowing us to separate the different contributions from \mathbf{M} and \mathbf{N} to transport effects such as SMR. Therefore, α -Fe₂O₃ represents a nice antiferromagnetic material platform, enabling us to characterize the electrical induced magnetic dynamics by comparing to field induced switching.

We grew α -Fe₂O₃ films on α -Al₂O₃ (0001) substrates with magnetron sputtering and post-deposition annealing. As is shown in Fig. 1b, despite the substantial lattice mismatch ($\sim 5.8\%$ in-plane), epitaxial α -Fe₂O₃(0001) films were obtained. The magnetization hysteresis curves measured with a SQUID magnetometer at 300 K are illustrated in Fig. 1c, which show a small M_s around 1.5~2 emu/cc and a coercive field of 500~1000 Oe within the entire thickness range (10~120 nm), consistent with the reported values in previous literatures^{18,19}. In order to study current-induced switching and observe the SMR, we sputter 5 nm Pt on the 10 nm α -Fe₂O₃ film and fabricate Hall bars with 4~20 μm width (Fig. 1d). Both longitudinal (R_{long}) and transverse resistances (R_H) were measured with a rotating external field in the film plane, which aligns the Néel vector perpendicular to the field orientation (Fig. 1e and f). Consistent results have been obtained from R_{long} and R_H measurements after taking into account of different geometrical factors in those two configurations. In the following, we will mostly focus on R_H measurement for

monitoring magnetic ordering. Close to saturation, the transverse SMR curves can be fitted by $R_H = \frac{\Delta R_H}{2} \sin(2\theta)$, where θ is the field angle defined in Fig. 1d. Our SMR signal is consistent with previous findings in other antiferromagnetic insulators such as NiO and Cr₂O₃²⁰⁻²³: the longitudinal SMR reaches maximum when N is collinear with current I . This sign is opposite to the SMR signal expected from a ferromagnetic material through the residual M , suggesting the dominant role of Néel vector in the SMR effect. The magnitude of SMR ($\Delta R_{\text{long}}/R_{\text{long}} \sim 0.06\%$) is also comparable to the earlier reports in NiO^{20,21}.

We first tested the current-induced 90° Néel vector switching by following the procedures in Ref. 8 and 10. As is shown in Fig. 2a, we send large current pulses that are oriented -45° (step A) and $+45^\circ$ (step B) from the horizontal direction to induce possible switches on the Néel vector. According to the current-induced spin-orbit torque picture, this would flip the Néel vector along the two orthogonal directions. To monitor the possible switching, we record the transverse SMR signal R_H after each pulse. To minimize the thermally induced resistance variation, R_H is read after 10 s of waiting, allowing the device to return to equilibrium. As is shown in Fig. 2b, a periodic change in R_H values is indeed observed (Fig. 2b). R_H repeatedly switches between the low and high values after setting and resetting current pulses and forms zigzag patterns, which is very similar to the switching characteristics reported earlier in NiO⁸⁻¹¹.

The biggest advantage associated with using α -Fe₂O₃ for spin torque switching lies in the easiness of controlling the Néel vector with external field. Therefore, to check if the observed switchings have magnetic origins, we compared the R_H switching both under zero magnetic field and under external field of $H_x = 2000$ Oe. As is shown in Fig. 2c, across the whole current range of 39~45 mA, the switching behaviors under these two situations are very similar. The minor differences in the exact R_H between the two curves are smaller than run-to-run variations under the

same field situation. From this comparison, we see that the applied field, which is supposed to align Néel vectors and suppress the current-induced switching, turns out to have little influences on the resistance change.

We further tried to understand the relationship between the resistance change and magnetic switching by determining the magnetic states after current application. This is done by measuring the angle-dependent SMR curves after a series of pulses. In principle, if the switching behavior of Fig. 2b and c comes from the reorientation of Néel vector, the SMR value after these pulses would correspond to a peak or valley position in the following angle-dependent SMR curve. However, in reality we found no change in the SMR signal, which always starts from zero and oscillates identically as field rotates, regardless of the magnitude and direction of prior current pulses (Fig. 2d and e). The only effect of the pulses is to cause an overall positive or negative shift in SMR curves. With large pulses, this shift can become even larger than the full range of field induced SMR (Fig. 2e). The independence between current-induced R_H switching and Néel vector orientation change suggests that the switching has a pure resistive origin. In our experiment, the current-induced temperature change of our devices can be as high as ~ 100 K (see supplementary information) due to the large current density ($\sim 6 \times 10^7$ A/cm²), which is comparable to the one that causes electromigration effects in Pt wire²⁴. Previously electromigration-induced memristive switching similar to those in Fig. 2b and c has been reported in various metallic wires^{24,25}. Therefore, cautions have to be paid in utilizing the sawtooth resistance switching feature as an evidence for antiferromagnetic switching.

The overall resistance shift caused by current pulses represents an obstacle in revealing current induced magnetic switching. To overcome this difficulty and search for possible current induced magnetic dynamics, we designed a new experiment which allows to demonstrate the

magnetic switching tendency with lower applied currents. We measured the angle-dependent SMR curve under an in-plane rotating field by applying different sensing currents. If there is a current-induced field or torque effect which tends to switch the magnetic ordering, the Néel vector will be tilted away (or toward) the current direction. These will be reflected in a deviation from the original field angle dependence of the SMR signal, from which we could extract the nature and magnitude of current's influence (Fig. 3a). Since we are focusing on the relative change of the SMR curve, the overall shift due to resistive switching as in Fig. 2 does not make contributions. Besides the current effect, we find that our α -Fe₂O₃ film always exhibits an easy-axis anisotropy energy of ~ 900 erg/cm³ within the basal plane due to the broken symmetry induced by the substrate, which favors $[\bar{1}2\bar{1}0]$ as an easy axis for the Néel vector \mathbf{N} (see supplementary information for detail). We take into account the influence from this constant, in-plane magnetic anisotropy in the following analysis on current-induced magnetic tilting.

The evolution of SMR signal with different currents applied along the x direction is shown in Fig. 3b. The 2 mA curve is used as a baseline for its low current density ($\sim 4 \times 10^6$ A/cm²). As current increases, the field angle (θ_H) corresponding to the peak and valley locations of SMR curves shifts toward the x axis (0 and 180° direction), suggesting that the current tends to align \mathbf{M} along y axis. Using $R_H = \frac{\Delta R_H}{2} \sin(2\theta_M)$, we can correlate SMR measured in Fig. 3b with the magnetic moment orientation θ_M . The current induced Néel vector tilting can therefore be characterized by the relative angle between \mathbf{M} and \mathbf{H} (which is $\theta_M - \theta_H$) as a function of θ_H , as is plotted in Fig. 3c. We note that within the first half of the period ($\theta_H = 0 \sim 90^\circ$), $\theta_M - \theta_H$ has negative values under the lowest applied current (2 mA), which can be explained by the intrinsic basal plane anisotropy that favors y axis for \mathbf{N} . As current increases, $\theta_M - \theta_H$ becomes less negative and at 20 mA it even switches sign, suggesting that current's effect is dominant over the intrinsic basal plane

anisotropy and x axis becomes more energetically favorable for N . We verified that this effect remains the same under the reversal of current direction. However, when the current direction is rotated by 90° , its influence on magnetic anisotropy changes sign and it now increases the intrinsic basal plane anisotropy by tilting N further toward the y axis (Fig. 3d).

In the measurement of Fig. 3b to d, the applied current always tends to align \mathbf{M} perpendicular to its direction (or equivalently, align N parallel with it). This trend is consistent in sign with the effect of current-induced Oersted field. However, the Oersted field is more than an order of magnitude smaller compared with the field strength needed for the observed effect (see supplementary information). Besides Oersted field, we can also exclude the Joule heating induced overall temperature increase as the mechanism for magnetic moment tilting. The magnetic anisotropy change due to the overall temperature increase should be a simple function of temperature and will have the same sign for currents applied along x and y axis, which is contradictory to our observation.

To answer the question whether the observed phenomena are due to spin-orbit torque, we modelled spin torque's influence onto the dynamics of antiferromagnet. The magnetic dynamics of collinear antiferromagnets can be described by a pair of coupled LLG equations on the two sublattices $\mathbf{m}_{A,B}$ (see supplementary information). Inside the LLG equations, the field-like torque on the two sublattices add destructively so only has negligible effect^{26,27}. However, the damping-like torque on the two sublattices $\boldsymbol{\tau}_{A,B}^{DL} = \tau_{DL} \mathbf{m}_{A,B} \times (\hat{\sigma} \times \mathbf{m}_{A,B})$ can add constructively and lead to observable effect. We solved the LLG equations numerically to find the equilibrium position of \mathbf{M} and N under applied currents. We find that while the damping-like torque does modify the equilibrium orientation of N (Fig. 3e), the induced in-plane tilting is not only smaller in magnitude,

but also has opposite sign with what we observed. Therefore, spin-orbit torque is likely not the root cause of the measured effects in Fig. 3.

Another evidence that the observed phenomena do not have a spin torque origin comes from the comparison of devices with different dimensions. In principle, spin torque is proportional to the current density J inside the heavy metal layer, and should not depend on the device dimension. In Fig. 4a, we plotted the magnetic moment tilting angle $\theta_M - \theta_H$ for three devices with channel width w of 4, 10 and 20 μm , respectively. We first kept the current density J the same between the 4 μm and 10 μm devices and found that the wider one has a much larger tilting angle. We then conduct measurements by keeping the device temperature T ($\propto J^2 w$, see supplementary information) the same and the current density different between the 10 μm and 20 μm devices. We saw that due to similar heating conditions, the current induced tilting becomes very close in this group of control samples. The fact that the effect strongly depends on the temperature instead of current density strongly suggests that it originates from a thermal mechanism.

While an overall temperature increase cannot cause the measured moment tilting, the Joule heating can lead to an additional effect that affects the magnetic anisotropy through the magnetoelastic coupling, which is a significant factor in antiferromagnets. Because of the long strip shape of the current channel, the stress induced by substrate thermal expansion around the device has an anisotropic distribution, as is shown schematically in Fig 4b. The compressive stress along x -axis is much stronger than along y -axis. By using thermal-mechanical finite element simulation (see supplementary information for details) (Fig. 4c), we determined that the average in-plane anisotropic stress $\Delta\sigma = \sigma_x - \sigma_y$ over the Hall cross region is ~ 40 MPa for the applied 20 mA current in Fig. 3. Besides, similar to other antiferromagnetic insulators, $\alpha\text{-Fe}_2\text{O}_3$ has a fairly large magnetoelastic effect^{28,29} with the magnetostrictive coefficient λ_s on the order of 10^{-6} . The

magnetoelastic energy due to thermal stress can therefore be written²⁸ as a function of $\Delta E_\sigma = 2\lambda_s\Delta\sigma$. On the other hand, based on the results in Fig. 3, we calculated the measured anisotropy energy change ΔE (see supplementary information) and plotted it as a function of applied current, which has a dependence of $\Delta E = aI^2$ (Fig. 4d). By equating the two energies and using $\Delta\sigma$ obtained from simulations under each applied current, we can determine λ_s in our α -Fe₂O₃ to be $\sim 1.4 \times 10^{-6}$, which is in the same order of magnitude with the reported values in previous studies^{28,29}. Using this determined magnetostrictive coefficient, we find that the results obtained from the whole range of the device widths as well as under different applied current direction and magnitude, can all be well explained (see supplementary information).

The dominance of thermally-caused magnetoelastic effect may also exist in current-induced magnetic switching experiments of other antiferromagnetic insulators with high magnetostrictive coefficient (e.g., $\lambda_s \sim 10^{-4}$ in NiO^{31,32}). To explore the real signature of spin-orbit torque induced dynamics in antiferromagnetic system, one needs to further suppress the anisotropic thermal stress in the device. As our results suggested, one possible approach is to scale the device down to the deep nanometer regime, which can maintain a high current density and at the same time reduce the total thermal load.

References

1. Wadley, P. *et al.* Electrical switching of an antiferromagnet. *Science* **351**, 587–590 (2016).
2. Grzybowski, M. J. *et al.* Imaging Current-Induced Switching of Antiferromagnetic Domains in CuMnAs. *Phys. Rev. Lett.* **118**, 057701 (2017).
3. Godinho, J. *et al.* Electrically induced and detected Néel vector reversal in a collinear antiferromagnet. *Nat. Commun.* **9**, 4686 (2018).
4. Jungwirth, T. *et al.* Writing and reading antiferromagnetic Mn₂Au by Néel spin-orbit torques and large anisotropic magnetoresistance. *Nat. Commun.* **9**, 348 (2018).
5. Zhou, X. F. *et al.* Strong Orientation-Dependent Spin-Orbit Torque in Thin Films of the Antiferromagnet Mn₂Au. *Phys. Rev. Appl.* **9**, 054028 (2018).
6. Meinert, M., Graulich, D. & Matalla-Wagner, T. Electrical Switching of Antiferromagnetic Mn₂Au and the Role of Thermal Activation. *Phys. Rev. Appl.* **9**, 064040 (2018).
7. Bodnar, S. Y. *et al.* Imaging of current induced Néel vector switching in antiferromagnetic Mn₂Au. *Phys. Rev. B* **99**, 140409 (2019).
8. Moriyama, T., Oda, K., Ohkochi, T., Kimata, M. & Ono, T. Spin torque control of antiferromagnetic moments in NiO. *Sci. Rep.* **8**, 14167 (2018).
9. Chen, X. Z. *et al.* Antidamping-Torque-Induced Switching in Biaxial Antiferromagnetic Insulators. *Phys. Rev. Lett.* **120**, 207204 (2018).
10. Baldrati, L. *et al.* Mechanism of Néel order switching in antiferromagnetic thin films revealed by magnetotransport and direct imaging. Preprint at <https://arxiv.org/abs/1810.11326> (2018).
11. Gray, I. *et al.* Spin Seebeck imaging of spin-torque switching in antiferromagnetic Pt/NiO heterostructures. Preprint at <https://arxiv.org/abs/1810.03997> (2019).

12. Liu, L., Lee, O. J., Gudmundsen, T. J., Ralph, D. C. & Buhrman, R. A. Current-induced switching of perpendicularly magnetized magnetic layers using spin torque from the spin hall effect. *Phys. Rev. Lett.* **109**, 096602 (2012).
13. Garelo, K. *et al.* Symmetry and magnitude of spin-orbit torques in ferromagnetic heterostructures. *Nat. Nanotechnol.* **8**, 587-593 (2013).
14. Hayashi, M., Kim, J., Yamanouchi, M. & Ohno, H. Quantitative characterization of the spin-orbit torque using harmonic Hall voltage measurements. *Phys. Rev. B* **89**, 144425 (2014).
15. Williamson, S. J. & Foner, S. Antiferromagnetic Resonance in Systems with Dzyaloshinsky-Moriya Coupling; Orientation Dependence in α -Fe₂O₃. *Phys. Rev.* **136**, A1102–A1106 (1964).
16. Elliston, P. R. & Troup, G. J. *Some antiferromagnetic resonance measurements in α -Fe₂O₃*. *Journal of Physics C: Solid State Physics* **1**, 169-178 (1968).
17. Lebrun, R. *et al.* Tunable long-distance spin transport in a crystalline antiferromagnetic iron oxide. *Nature* **561**, 222–225 (2018).
18. Flanders, P. J. & Remeika, J. P. Magnetic properties of hematite single crystals. *Philos. Mag.* **11**, 1271–1288 (1965).
19. Shimomura, N. *et al.* Morin transition temperature in (0001)-oriented α -Fe₂O₃ thin film and effect of Ir doping. *J. Appl. Phys.* **117**, 17C736 (2015).
20. Hoogeboom, G. R., Aqeel, A., Kuschel, T., Palstra, T. T. M. & Van Wees, B. J. Negative spin Hall magnetoresistance of Pt on the bulk easy-plane antiferromagnet NiO. *Appl. Phys. Lett.* **111**, 052409 (2017).
21. Fischer, J. *et al.* Spin Hall magnetoresistance in antiferromagnet/heavy-metal heterostructures. *Phys. Rev. B* **97**, 014417 (2018).
22. Baldrati, L. *et al.* Full angular dependence of the spin Hall and ordinary magnetoresistance in epitaxial antiferromagnetic NiO(001)/Pt thin films. *Phys. Rev. B* **98**, 024422 (2018).

23. Ji, Y. *et al.* Negative spin Hall magnetoresistance in antiferromagnetic Cr₂O₃/Ta bilayer at low temperature region. *Appl. Phys. Lett.* **112**, 232404 (2018).
24. Kozlova, T., Rudneva, M. & Zandbergen, H. W. In situ TEM and STEM studies of reversible electromigration in thin palladium-platinum bridges. *Nanotechnology* **24**, 505708 (2013).
25. Strachan, J. P., Strukov, D. B. & Borghetti, J. Memristive switching of single-component metallic nanowires. *Nanotechnology* **21**, 125204 (2010).
26. Železný, J., Wadley, P., Olejník, K., Hoffmann, A. & Ohno, H. Spin transport and spin torque in antiferromagnetic devices. *Nature Physics* **14**, 220–228 (2018).
27. Gomonay, O., Baltz, V., Brataas, A. & Tserkovnyak, Y. Antiferromagnetic spin textures and dynamics. *Nature Physics* **14**, 213–216 (2018).
28. Porath, H. Stress induced magnetic anisotropy in natural single crystals of hematite. *Philos. Mag.* **17**, 603–608 (1968).
29. Voskanyan, R. A., Levintin, R. Z. & Shchurov, V. A. Magnetostriction of a hematite monocrystal in fields up to 150 kOe. *Sov. Phys. JETP* **27**, 423–426 (1968).
30. Mandal, S., Menon, K. S. R., MacCherozzi, F. & Belkhou, R. Strain-induced nonequilibrium magnetoelastic domain structure and spin reorientation of NiO(100). *Phys. Rev. B* **80**, 184408 (2009).
31. Nakahigashi, K., Fukuoka, N. & Shimomura, Y. Crystal Structure of Antiferromagnetic NiO Determined by X-Ray Topography. *J. Phys. Soc. Japan* **38**, 1634–1640 (1975).
32. Weber, N. B., Ohldag, H., Gomonaj, H. & Hillebrecht, F. U. Magnetostrictive domain walls in antiferromagnetic NiO. *Phys. Rev. Lett.* **91**, 237205 (2003).

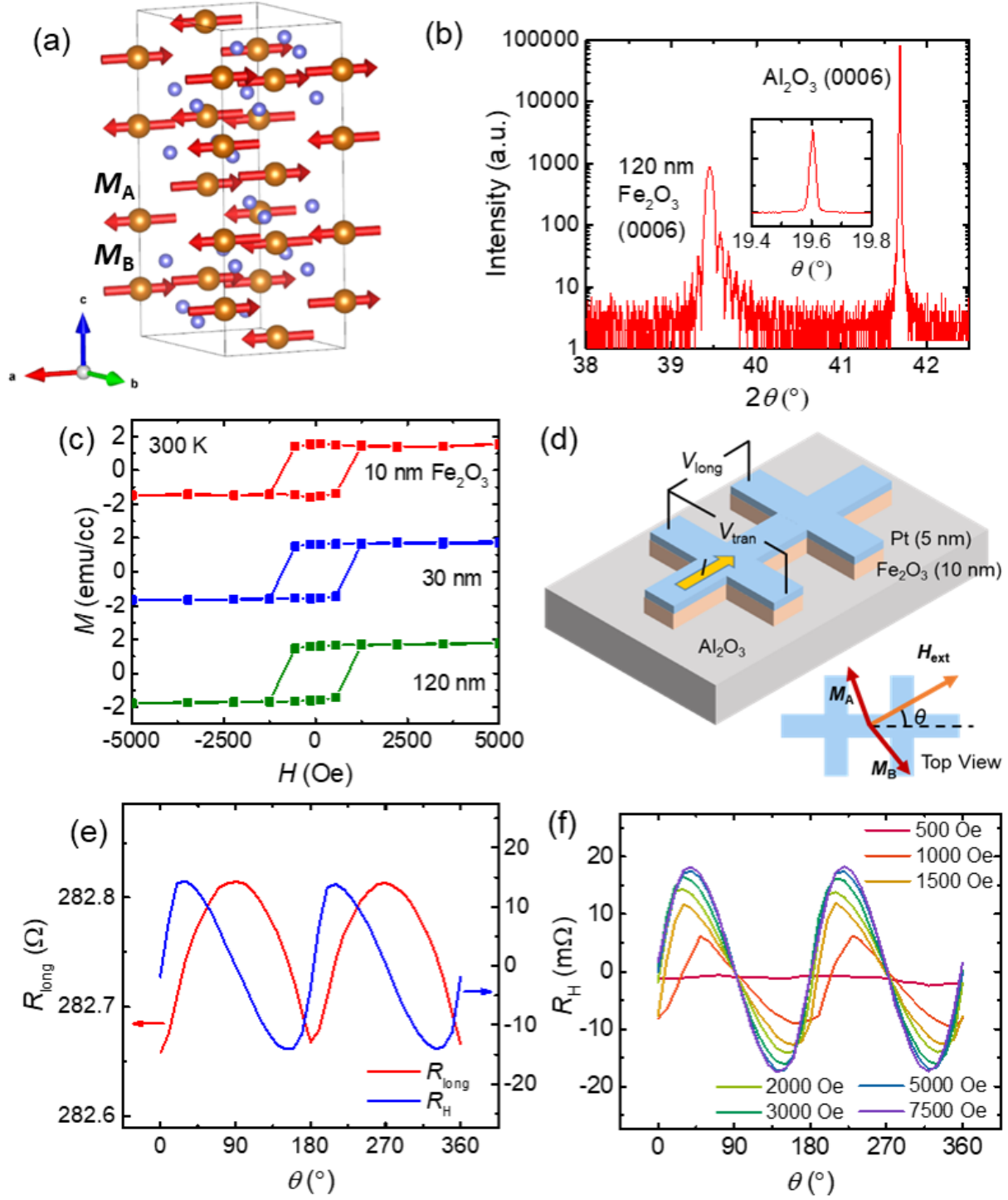


Figure 1 Material properties and spin Hall magnetoresistance of α - Fe_2O_3 . (a) Magnetic structure of α - Fe_2O_3 . Sublattices M_A and M_B are layer-stacked and antiparallel aligned with a small

canting angle (not visible in this figure). (b) X-ray diffraction of α -Fe₂O₃ (0001) film on α -Al₂O₃ (0001) substrate. Inset: rocking curve of the α -Fe₂O₃ (0006) peak. (c) SQUID magnetometry of α -Fe₂O₃ films for three different thicknesses. (d) Schematic of Hall bar device geometry and spin Hall magnetoresistance (SMR) measurement configuration. The inset shows the relative orientation between magnetic field and the canted moments of the two sublattices. (e) Longitudinal (R_{long}) and transverse (R_{H}) angle-dependent SMR with 2000 Oe in-plane field. The sensing current for this measurement is along $[\bar{1}2\bar{1}0]$ of the crystal. (f) Transverse angle-dependent SMR under different in-plane field.

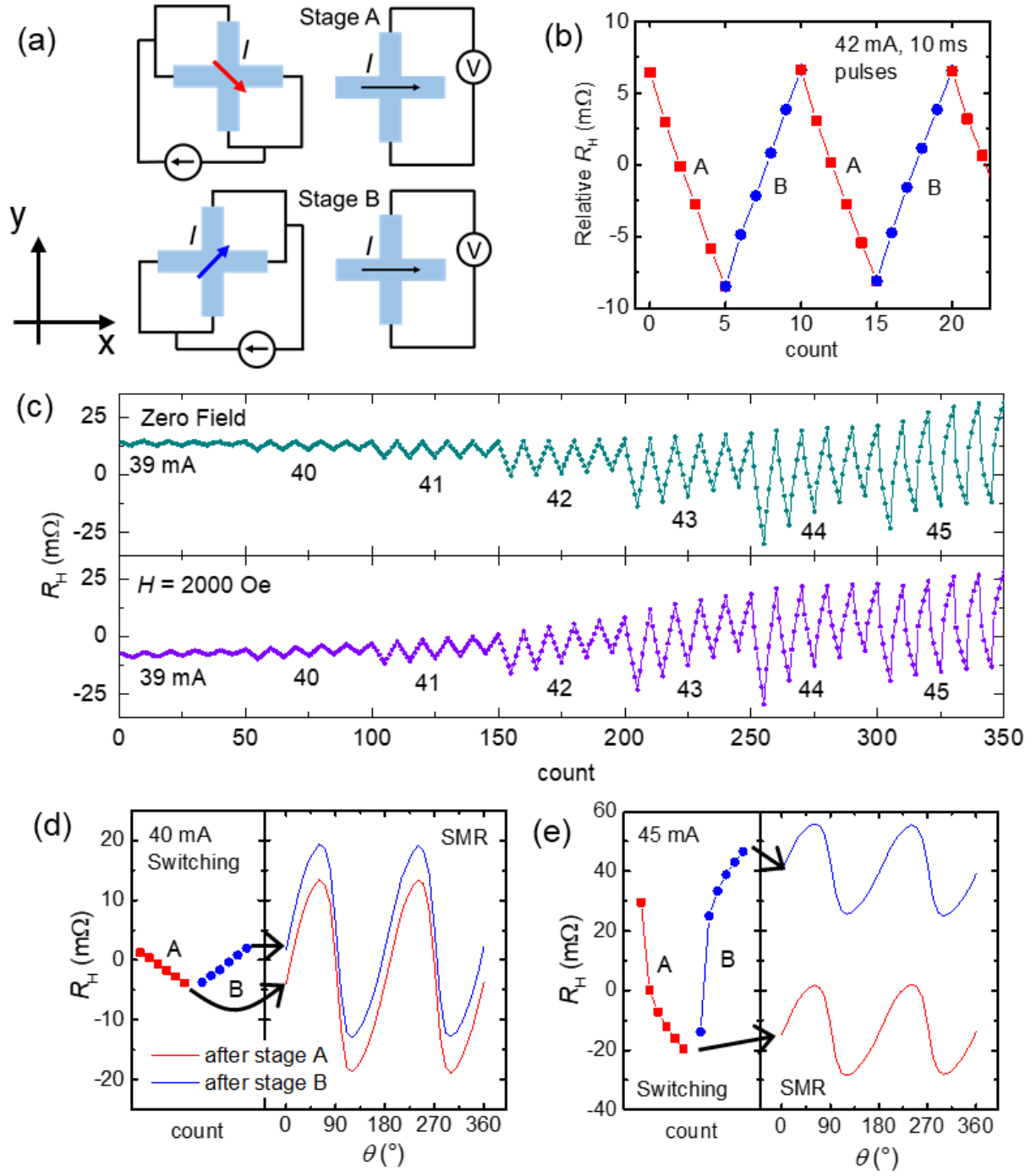


Figure 2 Current-induced Hall resistance switching in $\alpha\text{-Fe}_2\text{O}_3/\text{Pt}$ devices. (a) Schematics of the writing and reading procedure. In Stage A and Stage B, the net writing current pulse was applied along two diagonal directions, leading to low and high resistance states. (b) Example of

R_H switching by current pulses. The red branches represent measured SMR signal in Stage A and the blue branches are from Stage B. There are five pulses applied in each stage. (c) Current-induced switching without and with an external magnetic field of 2000 Oe. The field is applied parallel to x axis. (d) and (e) Measurement of angle-dependent SMR signal, showing the absence of correlation between the current-induced R_H switching and the SMR value change. (d) and (e) correspond to writing current of $I = 40$ mA and $I = 45$ mA, respectively.

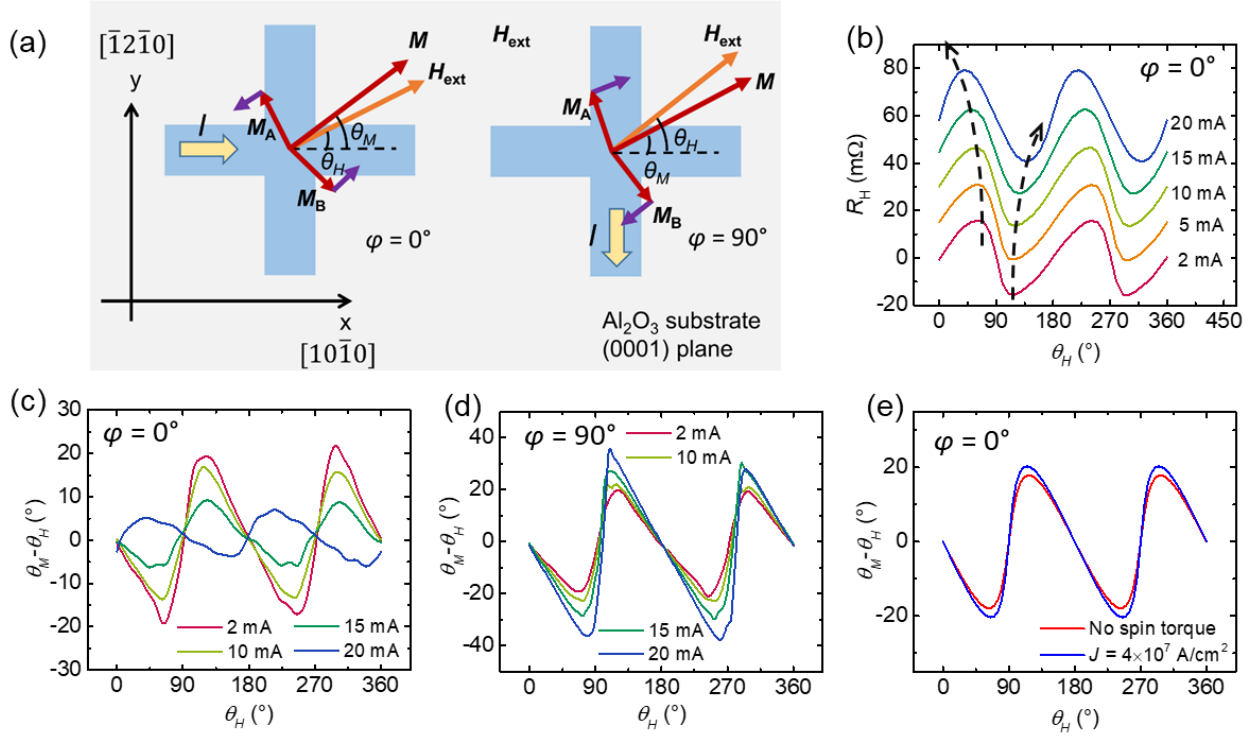


Figure 3 Current-induced magnetic order tilting as observed from SMR measurement. (a) Schematics of the magnetic moment tilting under applied currents. The left and right figures represent the cases when the current is applied along the x and y axis, respectively ($\varphi = 0^\circ$ and 90°). The purple arrows on the sublattice moments indicate the tilting direction. Intrinsic basal plane anisotropy is neglected in these schematics. (b) Angle-dependent SMR under different applied currents when I is parallel to x axis ($\varphi = 0^\circ$). The dashed arrows are guide for the eye, illustrating the shifting of peak and valley positions. (c) The angle between \mathbf{M} and \mathbf{H} as a function of θ_H for a range of applied currents at $\varphi = 0^\circ$. The curves are obtained from the results in Fig. (b). (d) The angle between \mathbf{M} and \mathbf{H} as a function of θ_H for a range of applied currents at $\varphi = 90^\circ$. (f) Spin torque induced magnetic moment tilting for current parallel to x axis ($\varphi = 0^\circ$), as is determined from macrospin simulation, which shows an opposite trend to the experiment results.

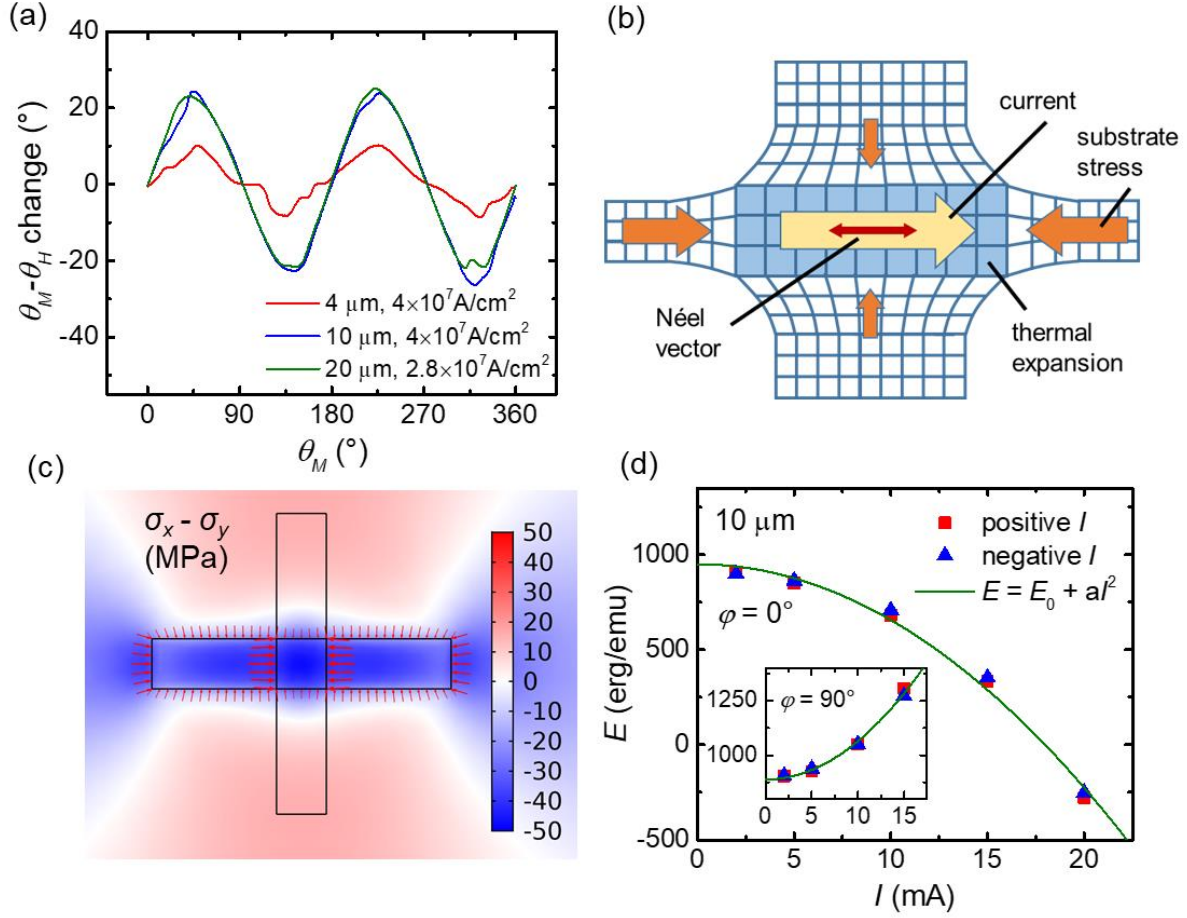


Figure 4 Thermal-magnetoelastic origin of the current-induced magnetic order tilting. (a)

The current induced magnetic moment tilting for devices with different channel width w . The background signal of θ_H and θ_M misalignment due to intrinsic basal plane anisotropy has been subtracted in these plots. (b) Schematic of the thermal-magnetoelastic switching. The current channel heats up the substrate and induces a thermal expansion, which has a larger magnitude in the longitudinal direction. Therefore, the resulting longitudinal compressive stress is stronger than the transverse one, leading to a current-induced easy axis anisotropy along the current flowing direction. (c) Finite-element simulation of the thermal-induced anisotropic compression on the substrate surface. Compressive stress is shown as negative. The small red arrows represent the magnitude and direction of the compressive stress. (d) The net easy axis anisotropy energy

within basal plane as a function of I when current applied along the x direction ($\varphi = 0^\circ$). A quadratic dependence of ΔE on I is obtained. The inset shows results from $\varphi = 90^\circ$ case.